Nanoscale

PAPER

View Article Online
View Journal | View Issue

Cite this: *Nanoscale*, 2023, **15**, 18423

Tuneable-by-design copper oxide nanoparticles in ionic liquid nanofluids†

Claire Boudie,[a] Manuel Maréchal,[b] Guillaume Ah-Lung,[c] Johan Jacquemin[a,c] and Peter Nockemann *[a]

Received 18th August 2023,
Accepted 15th October 2023

DOI: 10.1039/d3nr04159j

rsc.li/nanoscale

In this study, copper oxide nanoparticles (CuO-NPs) were synthesised in an ionic liquid, $[C_2MIm][C_nH_nCO_2]$, and the respective copper(II) carboxylate precursors. Heating the solution to 120 °C caused a colour change from blue to red, indicating a change in copper salt coordination and nanoparticle formation. Crystallography and UV-Vis spectroscopy were used to monitor the transition upon temperature changes. The particle formation was characterised using TEM and SWAXS analyses. The results showed that different anion chain lengths led to different particle sizes. When using copper(II) acetate precursors, the transformation resulted in CuO(I,II) clusters (<1 nm), depending on the imidazolium-based cation used. However, using a copper(II) octanoate precursor, small CuO-NPs in the range of 10–25 nm were formed, while larger CuO-NPs were obtained using a copper(II) butanoate precursor in the range of 10–61 nm.

Introduction

Transition metal oxides have a wide range of applications, including catalysis, sensing, energy storage, optics, and electronics.[1–4] The transformation of metal oxides into nanoscale materials is providing new properties in comparison with bulk materials, such as changes in their electronic properties, mechanical plasticity, magnetic behaviour, and phase-transition temperatures.[5] In recent years, nanoparticles have found major industrial applications in catalysis, polymer composites, optoelectronics, paints/coatings, and cosmetics.[2,6,7] Copper oxide nanoparticles, in particular, have numerous applications in solar cells, gas sensing, magnetic storage media, nanodevices, heterogeneous catalysts, and superconductors.[8–12]

Ionic liquids (ILs) have been employed in several studies for the formation of nanoparticles (NPs).[13–20] ILs are compounds composed entirely of cations and anions, having a melting point below 373 K (100 °C). They exhibit unique properties, such as low vapor pressure, a wide liquid-phase range, and high thermal and chemical stability. ILs can play an important role in the formation of nanomaterials, for example, as a stabilizer of nanoparticles.[16] The cation often acts as a stabilizing agent but can also function as a templating agent due to its tuneable surface tension, leading to an emulsion process that can influence the size of the nanoparticles. The role of emulsions as templates during nanoparticle formation has been well described in the synthesis of spherical silica particles. Furthermore, IL viscosity is known to affect the nanoparticle size due to slower mass transport in higher viscosity liquids. Thus, the more viscous the IL, the smaller the nanoparticles and *vice versa*.

Nanofluids are nano-scaled colloidal suspensions consisting of solid particles, rods, fibres, or tubes dispersed in different base fluids such as water, ethylene glycol, glycerol, engine oil, or ILs.[21,22] These materials can be used as solvents, catalysts, heat transfer fluids, magnetic fluids, lubricants, and luminescent materials, for the conservation of artworks, as novel electrolytes for batteries and organic solar cells, or in medical equipment.[23–29] This study focuses on the production and characterization of copper oxide-based nanofluid dispersions using ILs as the base fluids.

Previous work has shown that acetate-based ILs, in the presence of water, can be used for the *in situ* synthesis of copper(II) oxide nanoparticles, resulting in the formation of highly stable nanofluids.[30] This research also revealed the influence of the cation on the formation of copper oxide NPs, highlighting the contrasting properties of hydrophilic, aromatic $[C_4MIm][CH_3CO_2]$ and rather hydrophobic, aliphatic $[P_{88812}][CH_3CO_2]$ cations. The acetate anion acted here as a base and stabilising agent, enabling the preparation of stable NP dispersions in ILs (nanofluids). Other research demonstrated that binary mix-

[a]*The QUILL Research Centre, Queen's University Belfast, Stranmillis Road, Belfast, Northern Ireland, BT9 5AG, UK. E-mail: p.nockemann@qub.ac.uk*
[b]*Univ. Grenoble Alpes, CNRS, CEA, IRIG-SyMMES, 38000 Grenoble, France*
[c]*MSN Department, Mohammed VI Polytechnic University (UM6P), Lot 660 – Hay Moulay Rachid, 43150 Benguerir, Morocco*

† Electronic supplementary information (ESI) available. CCDC 2289136–2289139. For ESI and crystallographic data in CIF or other electronic format see DOI: https://doi.org/10.1039/d3nr04159j

tures of water and octanoate-based ILs form stable emulsions, in contrast to those based on the acetate anion, resulting in a reorganisation of the IL structure in the presence of water.[31,32] However, carboxylate-based IL structures and their interactions with metal-containing precursors, such as copper(II) butanoate and copper(II) octanoate, have not been studied previously. Thus, this project aims to examine in greater detail the interactions of these three carboxylate anions: acetate, butanoate, and octanoate-based ILs with water in the presence of copper(II) acetate, butanoate, and octanoate precursors, in order to understand the influence of interaction changes on the formation of CuO particles in IL-based media. The formation of copper(II) oxide nano-dispersions in these ILs can be used as a model-system for more complex systems. This work provides new insights into controlling CuO nanoparticle size and properties by tuning the ionic liquid anion structure. The ability to precisely design CuO nanoparticle characteristics through ionic liquid selection enables optimisation for applications such as antimicrobial coatings, sensors, solar cells, and catalytic processes.

Results and discussion

Copper oxide nanoparticles have previously been synthesised by dissolving a metal salt precursor in an ionic liquid (IL) with a small amount of water, followed by heating the solution to 120 °C for approximately 30 minutes. This experiment demonstrated that a temperature of 120 °C is essential for the complete transformation of the copper salt into copper oxide nanoparticles (CuO-NPs). An intermediate stage can be observed at temperatures between 80 and 90 °C. In these reactions, water serves a dual purpose: acting as a co-solvent and providing a source of hydroxide ions (HO^-) generated by the basicity of the carboxylate anions (Fig. 1). In an instance where copper(II) acetate is dissolved in a $[C_2Mim][OAc]$ IL, an intermediate is isolated and characterised through single crystal X-ray structure determination after crystallization from concentrated solutions.

A fully balanced equation for the synthesis of CuO from a copper(II) carboxylate precursor dissolved in $[C_2MIm][C_nH_{2n+1}CO_2]$ involves the presence of water as follows, in eqn (1):

$$\begin{aligned} &2[C_2MIm][C_nH_{2n+1}CO_2] + Cu_2(C_nH_{2n+1}CO_2)_4 \cdot 2H_2O \xrightarrow{50\,^\circ C} \\ &[C_2MIm]_2[Cu_2(C_nH_{2n+1}CO_2)_4] + 2H_2O \xrightarrow{120\,^\circ C} \\ &2CuO + 2[C_2MIm][C_nH_{2n+1}CO_2] + 4(C_nH_{2n+1}CO_2H) \end{aligned} \quad (1)$$

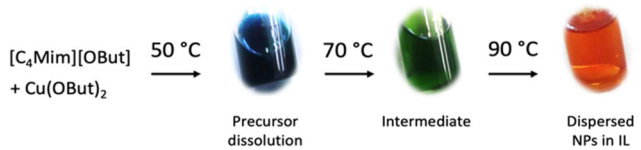

Fig. 1 Colour changes in the nanofluid formation from the precursor solution *via* intermediate formation to the copper oxide nano-dispersion (nanofluid).

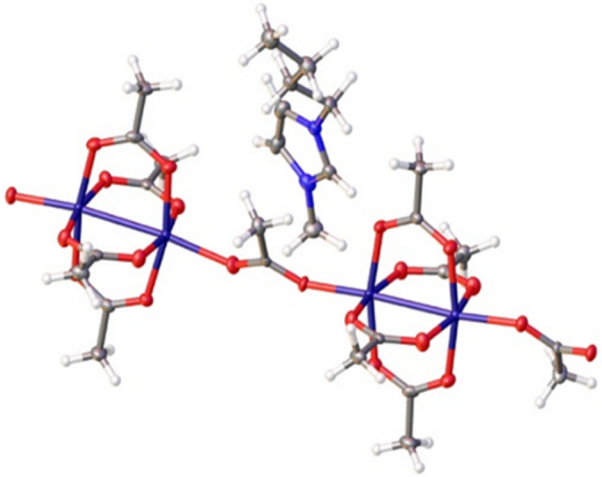

Fig. 2 Structure of $[C_4MIm][Cu_2(CH_3CO_2)_5]$, crystallised from the concentrated IL solution.

Solubility of copper(II) carboxylates in carboxylate ILs

Copper(II) acetate. Copper(II) acetate dihydrate demonstrates good solubility in acetate ILs. In aqueous solutions, copper(II) acetate adopts a paddle-wheel structure, $[Cu_2(CH_3CO_2)_4(H_2O)_2]$.[33] However, in ILs such as $[C_2MIm][CH_3CO_2]$, where abundant acetate anions are present, the coordinating water molecules of the paddle-wheel structure can be replaced by coordinating acetate groups. This resulted in the formation of a new compound, $[C_4MIm][Cu_2(CH_3CO_2)_5]$, which was isolated from a concentrated solution after heating it to approximately 50 °C, consisting of a coordination polymer crystallised from a concentrated solution of copper(II) acetate in the IL $[C_4MIm][CH_3CO_2]$, see Fig. 2. A reaction equation is given below in eqn (2):

$$\begin{aligned} &[C_4MIm][CH_3CO_2] + 2[Cu(CH_3CO_3)_2 \cdot H_2O] \rightarrow \\ &[C_4MIm][Cu_2(CH_3CO_2)_5] + H_2O \end{aligned} \quad (2)$$

Previously, Hinz *et al.* reported the crystal structure of a coordination polymer with bridging acetate anions.[34] However, both observed species are evidently solid-state species, and evidence from EXAFS suggests that paddle-wheel structures with partially substituted acetate coordination in the axial position are present in the solution. Swadzba-Kwasny *et al.* reported the formation of $[C_2MIm][Cu_3(CH_3CO_2)_5(H_2O)(OH)_2]\cdot H_2O$ (**1**), which is formed by heating a solution of $Cu_2(CH_3CO_2)_4\cdot(H_2O)_2$ in the IL $[C_2MIm][CH_3CO_2]$ to 80 °C and crystallizing the compound through slow cooling to room temperature.[30] The occurrence of the bridging hydroxyl group can be explained by the basicity of the acetate IL and the presence of a small amount of water derived from the coordinated H_2O in copper(II) acetate dihydrate. The structure of **1** consists of copper triangles coordinated to a shared HO^- group and bridged by acetate groups in mono- and bidentate modes. These trimeric hydroxy-clusters are then inter-

connected by acetate bridging to form a one-dimensional coordination polymer. A reaction (eqn (3)) is given below:

$$[C_2MIm][CH_3CO_2] + 2[Cu(CH_3CO_2)_2 \cdot H_2O] \rightarrow [C_2MIm][Cu_2(CH_3CO_2)_5(H_2O)(OH)_2] \cdot H_2O \quad (3)$$

Copper(II) butanoate and octanoate. The dissolution and speciation of copper(II) butanoate and octanoate in the corresponding ILs were also investigated. Therefore, $Cu(C_3H_7CO_2)_2$ and $Cu(C_7H_{15}CO_2)_2$ were synthesised and characterised. Copper(II) butanoate crystallised from a methanol solution and the crystal structure was determined, since the structure has not been previously reported. The crystal structure is shown in Fig. 3 and the crystal data are shown in Table 1. $Cu_2(C_3H_7CO_2)_4$ consists of a paddle-wheel structure; however, rather than consisting of isolated dimers as in the structure of the corresponding copper(II) acetate, this structure features a polymeric structure with the bridging carboxylates also bridging to the neighbouring dimers. This results in a 1-dimensional coordination polymer. The packing of $Cu_2(C_3H_7CO_2)_4$ is shown in the ESI.†

However, after dissolving copper(II) butanoate in the IL $[C_2MIm][C_3H_7CO_2]$, a highly concentrated solution was prepared. A crystalline product was obtained by heating the solution up to 80 °C and then allowing it to cool down slowly to room temperature. The crystal structure of this compound was determined to be $[C_2MIm]_2[Cu(C_3H_7CO_2)_4]$, as shown in Fig. 4. This structure comprises two $[C_2MIm]^+$ cations and isolated $[Cu(C_3H_7CO_2)_4]^{2-}$ anions. This result is surprising, considering that the corresponding acetate structures typically contain the paddle-wheel motif. The copper(II) $[Cu(C_3H_7CO_2)_4]^{2-}$ anions exhibit square-planar coordination with four monodentately coordinating butanoate groups. The packing in the crystal structure of $[C_2MIm]_2[Cu(C_3H_7CO_2)_4]$ is provided in the ESI.† The copper centres are packed along the *c*-axis; however, the distance between the copper metal centres is considerably large. The reaction (eqn (4)) is given below:

$$2[C_2MIm][C_3H_7CO_2] + Cu(CH_7CO_2)_2 \rightarrow [C_2MIm]_2[Cu(C_3H_7CO_2)_4] \quad (4)$$

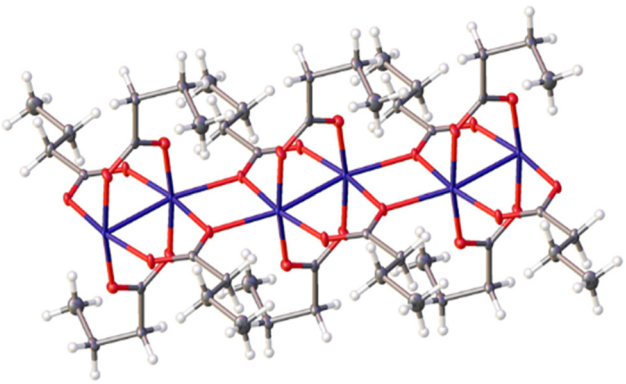

Fig. 3 Crystal structure of copper(II) butanoate, $Cu_2(C_3H_7CO_2)_4$.

Table 1 Crystal data for $Cu(C_3H_7CO_2)_2$, $[C_2MIm]_2[Cu(C_3H_7CO_2)_4]$ and $[C_2MIm]_2[Cu(C_7H_{15}CO_2)_4]$

Empirical formula	$CuC_8H_{14}O_4$	$CuC_{20}H_{39}N_2O_2$	$CuC_{38}H_{71}N_2O_2$
Formula weight	237.74 g mol^{-1}	403.08 g mol^{-1}	651.53 g mol^{-1}
Temperature/K	293(2)	100.00(10)	99.9(2)
Crystal system	Triclinic	Triclinic	Triclinic
Space group	$P\bar{1}$	$P\bar{1}$	$P\bar{1}$
a/Å	5.15600(12)	14.3866(6)	17.1050(4)
b/Å	8.6547(3)	15.9472(9)	17.4308(6)
c/Å	11.5154(3)	17.1521(8)	18.9701(6)
α/°	93.614(2)	65.732(5)	63.412(3)
β/°	93.5413(19)	77.128(4)	86.315(2)
γ/°	102.710(2)	67.803(5)	76.256(3)
Volume/Å^3	498.76(2)	3310.9(3)	4907.3(3)
Z	9	14	2
ρ_{calc}/g cm^{-3}	2.773	2.994	1.161
μ/mm^{-1}	10.582	9.875	1.027
F(000)	396.0	2898.0	1864.0
Radiation	Cu Kα (λ = 1.54184)	Cu Kα (λ = 1.54184)	Cu Kα (λ = 1.54184)
2Θ range for data collection/°	10.52 to 145.44	8.4 to 145.24	9.982 to 133.198
Index ranges	$-6 \le h \le 6$, $-10 \le k \le 10$, $-14 \le l \le 14$	$-17 \le h \le 14$, $-18 \le k \le 19$, $-20 \le l \le 20$	$-20 \le h \le 20$, $-20 \le k \le 18$, $-22 \le l \le 22$
Reflections collected	9209	22 643	84 986
Independent reflections	1969 [R_{int} = 0.0299, R_{sigma} = 0.0182]	12 772 [R_{int} = 0.0375, R_{sigma} = 0.0573]	17 300 [R_{int} = 0.0553, R_{sigma} = 0.0392]
Data/restraints/parameters	1969/0/120	12 772/0/755	17 300/0/1044
Goodness-of-fit on F^2	1.050	1.722	1.098
Final R indexes [$I \geqq 2\sigma(I)$]	R_1 = 0.0246, wR_2 = 0.0648	R_1 = 0.0821, wR_2 = 0.2502	R_1 = 0.1030, wR_2 = 0.2630
Final R indexes [all data]	R_1 = 0.0247, wR_2 = 0.0649	R_1 = 0.1011, wR_2 = 0.2625	R_1 = 0.1186, wR_2 = 0.2727
Largest diff. peak/hole/e Å^{-3}	0.36/−0.50	2.51/−0.92	1.76/−1.17

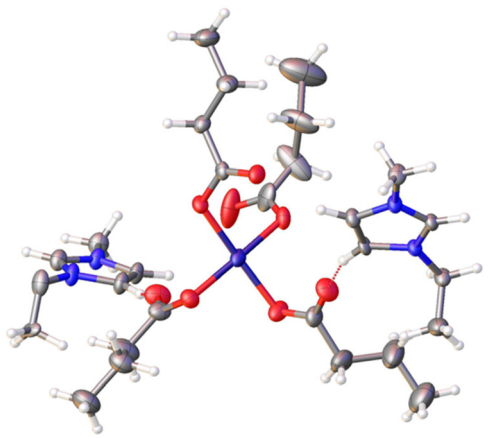

Fig. 4 Structure of $[C_2MIm]_2[Cu(C_3H_7CO_2)_4]$ showing one of the crystallographically independent Cu centres.

Copper(II) octanoate was synthesised and characterised; however, obtaining suitable crystals of the compound in methanol or any other solvent proved to be impossible. By dissolving $Cu(C_7H_{15}CO_2)_2$ in the IL $[C_2MIm][C_7H_{15}CO_2]$, a struc-

ture akin to $[C_2MIm]_2[Cu(C_3H_7CO_2)_4]$ was achieved. A highly concentrated solution was prepared at 80 °C and allowed to cool down slowly. The crystal structure of this compound was determined to be $[C_2MIm]_2[Cu(C_7H_{15}CO_2)_4]$, as shown in Fig. 5. Similar to the butanoate, this structure comprises two $[C_2MIm]^+$ cations and isolated $[Cu(C_7H_{15}CO_2)_4]^{2-}$ anions. The copper(II) $[Cu(C_7H_{15}CO_2)_4]^-$ anions exhibit a square-planar coordination with four monodentately coordinating octanoate groups. The packing of $[C_2MIm]_2[Cu(C_7H_{15}CO_2)_4]$ is illustrated in the ESI.† The copper centres and the cations are packed within one layer of the structure, separated by layers of the long alkyl chains arranged into another layer. A reaction (eqn (5)) is given below:

$$2[C_2MIm][C_7H_{15}CO_2] + Cu(C_7H_{15}CO_2)_2 \rightarrow [C_2MIm]_2[Cu(C_7H_{15}CO_2)_4] \quad (5)$$

The presence of water is crucial for CuO-NP formation, as demonstrated previously.[30] In binary mixtures using the same ILs as for the CuO-NP synthesis, water appears to reorganize the ILs up to a certain concentration limit, and then fully or partially dissociate into a $[C_2MIm]^+$ cation and a $[C_nH_{2n+1}CO_2]^-$ anion at higher concentrations. In this section, the impact of water on CuO-NP formation was investigated using Transmission Electron Microscopy (TEM) to determine the size distribution and shape of CuO-NPs at various compositions of the ternary mixtures (see Fig. 6 and 7). However, it was not feasible to add more than 0.65 mole fraction of water to the solution without forming a precipitate or dissolving all the copper salt.

Moreover, it was not possible to include less than 0.3 mole fraction of the IL to the solution for the same reasons. Furthermore, it has been shown that water concentration does not affect the size and morphology of the particles.

Copper oxide nanoparticle solutions were synthesised using a copper(II) butanoate precursor in $[C_2MIm][C_3H_7CO_2]$ and a copper(II) octanoate precursor in $[C_2MIm][C_7H_{15}CO_2]$. The particles derived from the copper(II) octanoate precursor yielded smaller CuO-NPs, ranging from 10 to 25 nm, compared to those from the copper(II) butanoate precursor, which ranged from 10 to 61 nm. CuO-NPs synthesised from copper(II) butanoate exhibited a maximum average diameter of around 45 nm, while those synthesised from copper(II) octanoate displayed an average diameter of approximately 15 nm. In our previous work, the copper(II) acetate precursor led to the formation of CuO(I,II) nanoclusters (less than 1 nm in size).[30] The nanoparticle size distribution is strongly influenced by either the IL-cation (as demonstrated in our previous work[30]) or the IL-anion (as proven in the present work). In this study, we revealed that altering the structure of the IL, for example, changing the anion from acetate to octanoate, also impacts the morphology of the resulting nanomaterials. This finding is significant, as controlling the morphology of transition metal oxides is challenging, and the concept could potentially be applied to other metal oxides, such as those of Fe, Mn, Co, Ni, and lanthanides.

The CuO nanofluids synthesised in this work were stable, as no precipitation or any aggregation issues were observed over months of storage.

Physical properties of copper precursors in the IL before/after turning into nanofluids. The solutions were analysed after the copper salts were dissolved at 50 °C in their respective ILs, and after the same solutions had turned into nanofluids at 120 °C.

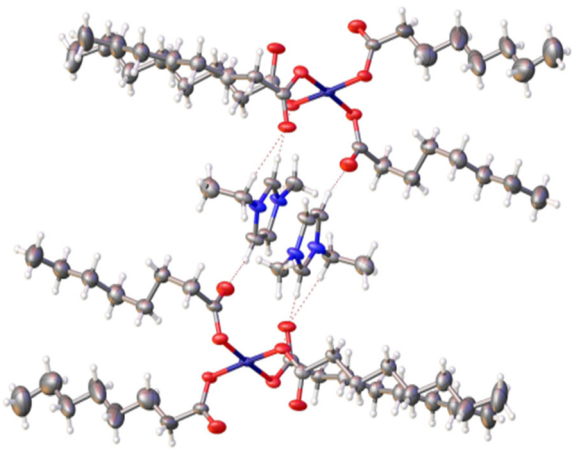

Fig. 5 Structure of $[C_2MIm]_2[Cu(C_7H_{15}CO_2)_4]$ formed by heating a solution of $Cu(C_7H_{15}CO_2)_2$ in the IL $[C_2MIm][C_7H_{15}CO_2]$ to 80 °C and crystallising the compound by slow cooling.

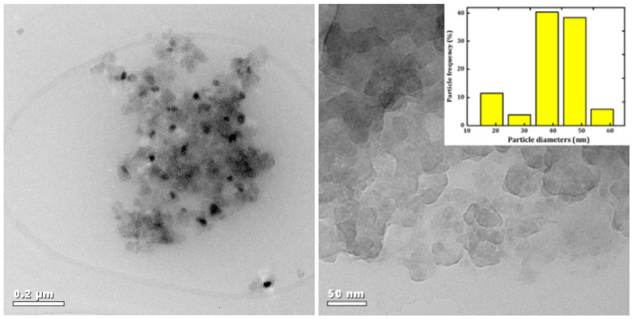

Fig. 6 TEM images of copper oxide nanoparticles synthesised in $[C_2MIm][C_3H_7CO_2]$ and a copper(II) butanoate precursor.

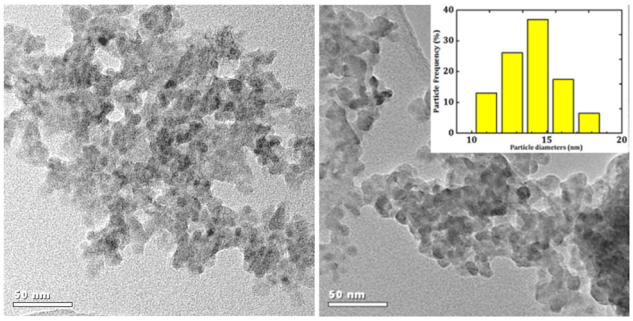

Fig. 7 TEM images of copper oxide nanoparticles synthesised in $[C_2MIm][C_7H_{15}CO_2]$ and a copper(II) octanoate precursor.

Density. All solutions containing copper salt or nanofluids exhibit higher density than their respective pure ILs. However, as the solutions transition into CuO-NPs, their densities decrease compared to those of their precursor solutions, indicating a change in the copper species present. Notably, the nanofluid solutions were consistently more fluid than the pre-reaction solutions. However, as the anion alkyl chain length increased, the density of the copper salt and nanofluid solutions approached that of the pure ILs. This phenomenon is likely attributable to the proportionally larger amount of copper ions present in the copper(II) acetate solution compared to the other two solutions. Fig. 8 shows the density data as a function of temperature. The experimental densities (ρ/g cm^{-3}) were correlated with temperature (T/K) using linear regression (eqn (6) and (7)), with the correlation parameters provided in Table 2 with raw data tabulated in the ESI (see Table S2†).

$$\rho = \sum_{i=0}^{1} b_i \times T^i \quad (6)$$

$$\sigma = \left[\frac{\sum (\rho_i^{exp} - \rho_i^{cal})^2}{n - \nu}\right]^{0.5} \quad (7)$$

ρ represents the density of the IL, b_i the linear fitting coefficients of the density, and T^i the temperature. σ represents the standard deviation, n the number of experimental points, and ν the number of adjustable parameters.

Viscosity. In Fig. 9, the nanofluid solutions are less viscous than the pure IL, apart from the solution made with copper(II) acetate precursors that show higher viscosity. However, the nanofluid solution made from the copper(II) octanoate precursor shows much higher viscosity than the nanofluid solution made with a copper(II) butanoate precursor. This could explain the smaller diameters of the CuO-NPs formed in the copper(II) octanoate precursor solution. Indeed, viscosity has already been shown to play an important role in the formation and stability of the NPs.

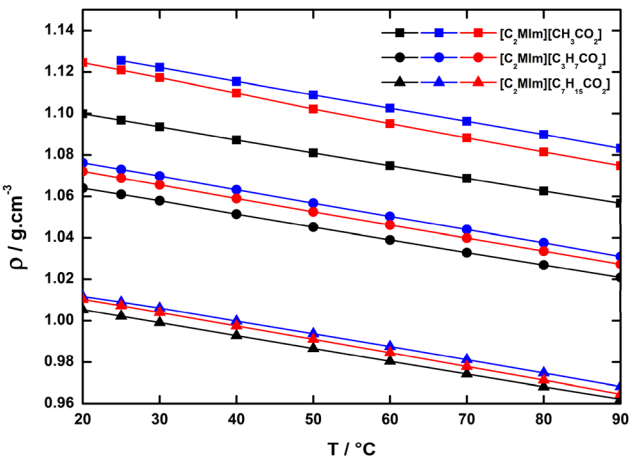

Fig. 8 Experimental density, ρ, as a function of the temperature and 0.1 MPa of the copper(II) carboxylate mixture for the pure IL (black), copper salt before turning into nanoparticles (blue), and the nanofluid solutions (red) from: [C_2MIm][CH_3CO_2]; [C_2MIm][$C_3H_7CO_2$]; and [C_2MIm][$C_7H_{15}CO_2$]. The lines represent linear type fitting of the experimental data (see Table S1 of the ESI†) with parameters reported in Table 2.

Table 2 Linear fitting coefficients b_i of the density of the ternary mixtures as a function of the temperature calculated from experimental data using the above equation along with their standard deviation

Solutions	b_0/g cm^{-3}	$10^4 \times b_1$/g cm^{-3} K^{-1}	$10^4 \times \sigma$/g cm^{-3}
[C_2MIm][CH_3CO_2]	1.2812	−6.1903	8.4
[C_2MIm][CH_3CO_2]-copper salt (blue)	1.3185	−6.4778	7.5
[C_2MIm][CH_3CO_2]-CuO-NPs (red)	1.3337	−7.1437	19
[C_2MIm][$C_3H_7CO_2$]	1.2452	−6.1827	8.4
[C_2MIm][$C_3H_7CO_2$] copper salt (blue)	1.2652	−6.4487	4.2
[C_2MIm][$C_3H_7CO_2$] CuO-NPs (red)	1.2595	−6.4000	7.0
[C_2MIm][$C_7H_{15}CO_2$]	1.1861	−6.1703	5.1
[C_2MIm][$C_7H_{15}CO_2$] copper salt (blue)	1.1944	−6.2157	12
[C_2MIm][$C_7H_{15}CO_2$]-CuO-NPs (red)	1.2018	−6.5247	5.8

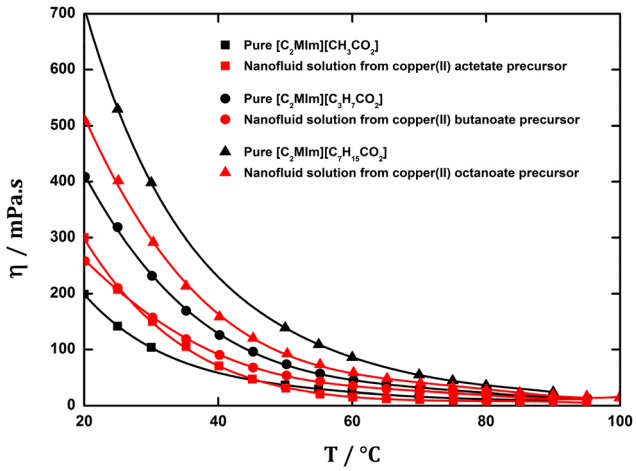

Fig. 9 Viscosity, η, of the pure ILs as a function of the temperature from 20 to 100 °C for pure ILs: ■, [C_2MIm][CH_3CO_2]; ✎, [C_2MIm][$C_3H_7CO_2$]; ➡, [C_2MIm][$C_7H_{15}CO_2$] and for the nanofluid solution from: ▪, copper(II) acetate precursor; ✎, copper(II) butanoate precursor; and ➡, copper(II) octanoate precursor; at 0.1 MPa. The lines represent a VFT-type fitting of the experimental data as reported in Tables S2 and S3 (see the ESI†).

Conductivity. The presence of CuO-NPs increases the conductivity of the solution. It is in accordance with the literature where most of the time NPs have been found to increase the conductivity of the system (Table 3). Furthermore, the conductivity dramatically decreases with the increase of the alkyl-chain length on the carboxylate anion. Therefore, the copper (II) octanoate seems to make better shaped NPs as seen from the TEM analysis; however, it would not be a relevant electrolyte in comparison with the nanofluids synthesised from copper(II) acetate.

Solubility study of the formation of copper oxide nanoparticles

UV-VIS spectroscopy. Plasmon resonance is a well-known characteristic of NP formation. It has been seen in many studies of NPs in UV-VIS spectra, mostly for gold

Table 3 Experimental conductivity, σ, and measurements of the nanofluid solutions as a function of composition at 0.1 MPa

Copper(II) precursor and pure IL used	σ/mS cm^{-1}of copper salt solutions	σ/mS cm^{-1}of nanofluid solutions
$[C_2MIm][CH_3CO_2]$-IL	2.77	—
Copper(II) acetate	2.14	2.79
$[C_2MIm][C_3H_7CO_2]$-IL	1.19	—
Copper(II) butanoate	0.78	1.08
$[C_2MIm][C_7H_{15}CO_2]$-IL	0.32	—
Copper(II) octanoate	0.19	0.28

nanoparticles,[35,36] and in the formation of copper-nanofluids. At room temperature, a solution of copper(II) octanoate in $[C_2MIm][C_7H_{15}CO_2]$ shows a blue coloured solution, with an absorption band at about 425 nm. The solution was then heated carefully to about 70 °C, where the colour changed to green, with an absorption band at about 425 nm. The results are shown in Fig. 10. Similarly, as for the copper(II) acetate, the green colour can only be observed for a few minutes, after the temperature is increased carefully. Further heating to 120 °C resulted in a deep red solution, exhibiting an absorption maximum at 445 nm.

The solution was then heated to 150 °C, showing a black colour that is due to the partial decomposition of the solution. A Plasmon band can also be found in the red absorption range, which is typical of nanoparticle formation. The shape of the absorption band is not as well defined as a typical plasmon band; however, the TEM of a sample of this solution proves the presence of NPs in the $[C_2MIm][C_7H_{15}CO_2]$ IL (see Fig. 6). Copper salt solutions in their respective ILs containing the same cation showed different absorption bands, depending on the temperature the solutions were heated to. For all solutions, nanofluids were observed at the highest absorbance, exhibiting a plasmon band typical of the presence of nanoparticles.

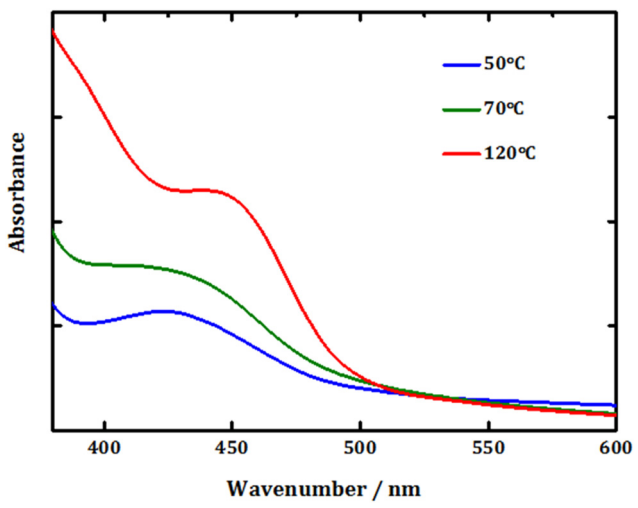

Fig. 10 *UV-VIS spectra:* Colour changes observed during the synthesis of nanofluids with copper(II) octanoate in $[C_2MIm][C_7H_{15}CO_2]$. The blue spectrum represents the solution at 50 °C; the green spectrum, the solution at 70 °C; and the red spectrum, the solution at 120 °C.

Small and wide-angle X-Ray scattering (SWAXS)

Going further, SWAXS experiments provided relevant insight into the molecular interactions in the studied liquid structures. No significant contributions were observed at low Q, excluding any long-range ordering which would reveal any long-range correlation in the ILs or/and a compact aggregation of the NPs, whereas contributions were present at higher Q in the pure and binary mixtures.

Influence of the alkyl chain length in the pure ILs. The local organisation of the three pure ILs, $[C_2MIm][CH_3CO_2]$, $[C_2MIm][C_3H_7CO_2]$ and $[C_2MIm][C_7H_{15}CO_2]$, was first separately investigated to figure out their intrinsic inter- and intramolecular interactions. The three pure ILs were compared to each other using the SWAXS diffraction patterns (Fig. 11) showing three groups of several characteristic lengths. Pure $[C_2MIm][CH_3CO_2]$ showed a wide bump around 7 nm^{-1}, called peak II, and combined contributions of inter- and intramolecular lengths, and a large scattering second contribution at 16.62 nm^{-1}, called peak III, assigned to neighbouring shells and intramolecular characteristic distances. In contrast, pure $[C_2MIm][C_3H_7CO_2]$ and pure $[C_2MIm][C_7H_{15}CO_2]$ showed significant pre-peaks at 5.2 and 3.34 nm^{-1}, respectively, and the second contribution at 15.75 and 15.43 nm^{-1}, respectively, as shown in Fig. 11. The pre-peaks indicate a self-organisation at the nanoscale.

The differences are seen in the Q-range with different positions of the characteristic distance distributions, which are lower in the case of $[C_2MIm][C_7H_{15}CO_2]$ than for $[C_2MIm][C_3H_7CO_2]$, and in the intensity of the pre-peaks which is much higher in the case of $[C_2MIm][C_7H_{15}CO_2]$ than for $[C_2MIm][C_3H_7CO_2]$. The shift toward higher Q in the second contribution shows shorter intra-molecular interactions in between anion pair atoms, adjacent tails, cation tails with pairs and cation atoms, when the anion alkyl chain length becomes shorter. As $[C_2MIm][CH_3CO_2]$ does not show any rele-

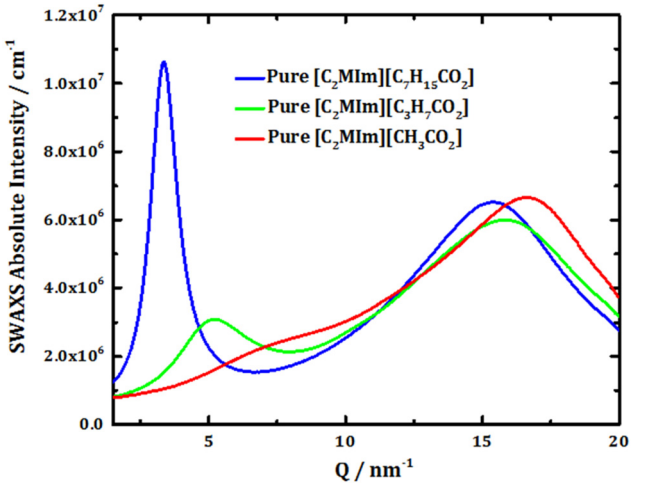

Fig. 11 SWAXS diffraction patterns of the pure ILs, with $[C_2MIm][CH_3CO_2]$ (red), $[C_2MIm][C_3H_7CO_2]$ (green), and $[C_2MIm][C_7H_{15}CO_2]$ (blue).

vant pre-peak between 3 and 6 nm^{-1}, and the intensity of the pre-peak observed increases with longer carbon chain lengths, this reveals that this pre-peak at low Q shows the inter-molecular interactions from the anion alkyl-chain length and its cation. These two contributions have been already described and reported in the case of others ILs.[37–39]

Influence of the copper salt precursor. The formation of copper oxide NPs was investigated in solutions containing a mixture of ILs (χ_{IL} = 0.95), copper precursors (χ_{Cu} = 0.05), and pure water. Fig. 12 shows that the addition of a copper salt precursor or CuO-NPs results in the restructuring of the acetate-based solutions, as evidenced by the emergence of a new pre-peak. In contrast, the butanoate-based solutions appear to become disorganised upon the addition of copper, causing the pre-peak to fade. This observation is further supported by the broad contribution arising from inter- and intra-molecular interactions, which confirms the reorganization of the ILs.

Interestingly, the addition of copper to the octanoate-based solutions does not disrupt their self-organization. The self-organised structure of $[C_2MIm][C_7H_{15}CO_2]$ is revealed by the repetitive patterns observed for all compositions, enabling NPs to intercalate into the same "free space" at any composition. The self-organised structure of the $[C_7H_{15}CO_2]$-based IL is attributed to its hydrophobic character and the strong van der Waals interactions between the anions and cations.

Additionally, the inability to determine NP size using SAXS can be explained by the low particle concentration, which complicates the extraction of form factors, especially when dealing with unfavourable differences in scattering-length densities (SLD).

Nanoparticle formation as a function of temperature. NP formation between 50 °C and 120 °C was investigated, in order to go further. Each sample of ternary mixtures was first well dissolved at 50 °C and then stored in a sample container. Each solution was kept in its own container during the whole experiment of X-ray scattering. The NP formation was thus *in situ* monitored *via* SWAXS patterns from 50 up to 120 °C. The SWAXS patterns of all three ILs and three studied compositions are shown in the figures below. A color code was used to represent the same composition at 50 and 120 °C.

The increase of the temperature for all ternary mixtures modifies the SWAXS patterns with a decrease of the absolute intensities, especially for the pre-peaks, and to a lesser extent a general shift to smaller Q, *i.e.* to larger characteristic lengths. This evolution is due to a thermal volume expansion while the second contribution is due to inter-atomic correlations. The decrease in intensity with the water concentration decrease is related to lower SLD.

More interestingly, these significant shifts towards low Q values are observed from 50 to 120 °C for the second contribution, whereas slight shifts are observed for the pre-peaks. This means that the intramolecular characteristic distances in the ILs become longer when NPs are added into the solutions. Concomitantly, NPs establish free spaces in between the anions and the cations of the ILs and are intercalated into the polar/non-polar nano-segregation of ILs.

However, the SWAXS patterns in Fig. 14 for $[C_2MIm][C_7H_{15}CO_2]$ appear repetitive for all compositions unlike those of the acetate (*cf.* ESI†) and butanoate anions (Fig. 13). This shows that even at high water concentration, the $[C_7H_{15}CO_2]^-$-anion-based solutions retain a highly organised structure that allows CuO-NPs to intercalate in the same way at any composition.

Influence of water on nanoparticle formation. SWAXS was used to study the influence of water on NP formation. Ternary mixtures of the three compositions (χ_{IL} = 0.95, 0.50 and 0.30) at 120 °C were plotted in the same graph for each respective IL and compared to the respective pure IL in order to look at the impact of the water concentration in the NP formation. Pure

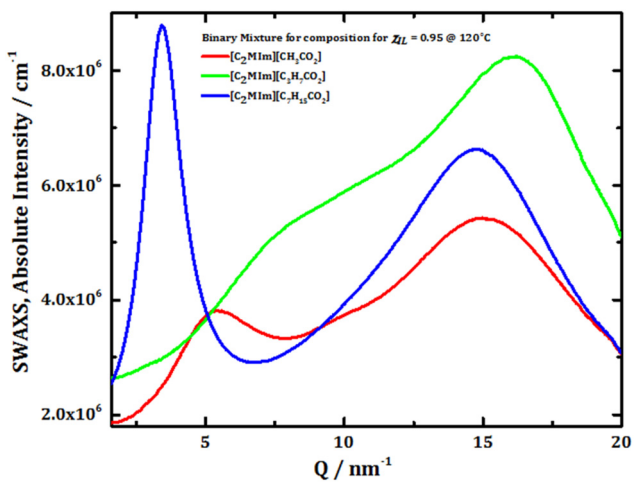

Fig. 12 SWAXS patterns of $[C_2MIm][CH_3CO_2]$ (red), $[C_2MIm][C_3H_7CO_2]$ (green), and $[C_2MIm][C_7H_{15}CO_2]$ (blue) at the composition χ_{IL} = 0.95 of the binary mixtures with water and the copper(II) carboxylate precursor at 120 °C.

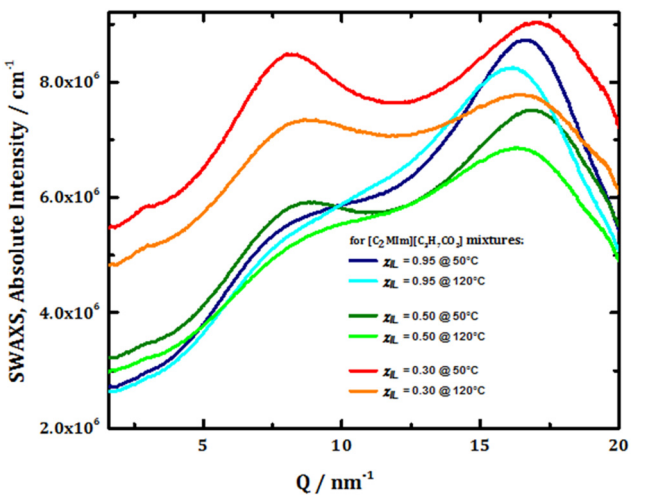

Fig. 13 SWAXS patterns of $[C_2MIm][C_3H_7CO_2]$ in binary and ternary mixtures with water and copper(II) butanoate at 50 °C for the compositions χ_{IL} = 0.95 (blue), χ_{IL} = 0.50 (green) and χ_{IL} = 0.30 (red), and at 120 °C for the compositions χ_{IL} = 0.95 (cyan), χ_{IL} = 0.50 (green) and χ_{IL} = 0.30 (orange).

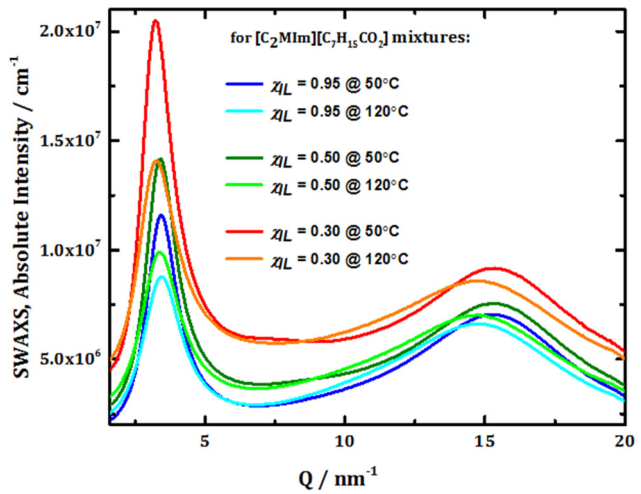

Fig. 14 SWAXS patterns of $[C_2MIm][C_7H_{15}CO_2]$ in binary and ternary mixtures with water and copper(II) octanoate at 50 °C for the compositions χ_{IL} = 0.95 (blue), χ_{IL} = 0.50 (green) and χ_{IL} = 0.30 (red), and at 120 °C for the compositions χ_{IL} = 0.95 (cyan), χ_{IL} = 0.50 (green) and χ_{IL} = 0.30 (orange).

$[C_2MIm][CH_3CO_2]$ (see Fig. 11) and binary mixtures with water show only a contribution at around 16.62 nm^{-1} (*cf.* ESI†). However, when adding a copper(II) acetate precursor to the solution, the SWAXS patterns at 120 °C reveal another pre-peak at around 5.50 nm^{-1} for all three ternary compositions. As a result, $[C_2MIm][CH_3CO_2]$ exhibits a nanoscale order after the addition and formation of CuO-NPs due to the formation of coulombic interactions. However, pure $[C_2MIm][C_3H_7CO_2]$ and its binary mixtures with water show already two contributions at around the same Q values than for the acetate (5.20 and 15.43 nm^{-1}) as shown in Fig. 15. Unlike $[C_2MIm][CH_3CO_2]$, $[C_2MIm][C_3H_7CO_2]$ gets significantly disordered at the nanoscale after the formation of CuO-NPs compared to its pure IL-related structure. Indeed, the pre-peak disappears since only a large bump is observed for compositions of 0.5 and 0.95 IL mole fractions. This new contribution arises from inter- and intramolecular characteristic lengths and is better defined at a composition of 0.3 mole fraction of the IL. This change, due to the loss of the polar/non-polar nano-segregation at the nanoscale, promotes correlations between anions, between the head group of the imidazolium ring and the anion, and between the methylene hydrogens and the anion (contributing negatively).

In contrast, the polar/non-polar segregation of $[C_2MIm][C_7H_{15}CO_2]$ remains at the nanometre scale before and after the formation of CuO-NPs due to its hydrophobic character and its strong van der Waals interactions (*cf.* Fig. 16). The second contribution is significantly shifted to a lower Q after the formation of CuO-NPs. This shows that in all presented solutions, CuO-NPs will fit in where there is space and therefore will be formed more instantly in the case of $[C_2MIm][C_7H_{15}CO_2]$ due to its highly organised nanostructure, forcing the NPs to "fit" in the same place. The octanoate-anion-based IL likely forms a capping layer on the surface of the NPs that disturbs the nanostructure of the IL and induces its restructuring by promoting the weak interactions.

Proposed mechanism of nanoparticle formation. The combination of all presented data and conclusions allows us to suggest a mechanism of CuO-NP formation in the case of the copper(II) octanoate precursor solutions. Since water addition into the ILs tends to dissociate both cations and anions, it forms a water shell surrounded by a $[C_7H_{15}CO_2]^-$-anion-based shell of the IL. The CuO-NPs would then be formed within the water shell as described in Fig. 17 and 18. Since the NPs were formed only inside the water shell, leaving then unaggregated

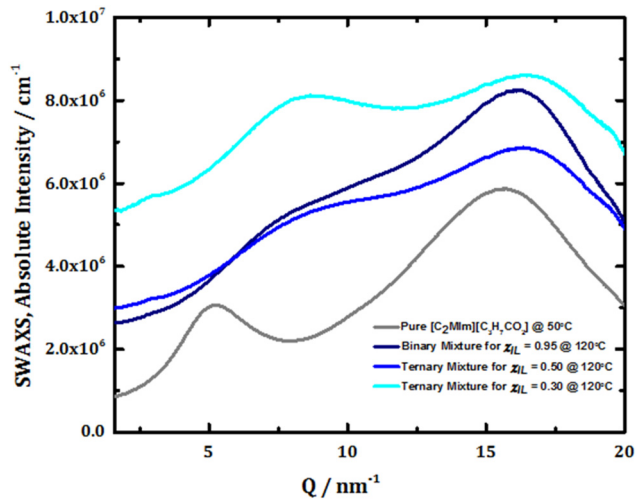

Fig. 15 SWAXS patterns of pure $[C_2MIm][C_3H_7CO_2]$ (grey), and its binary and ternary mixtures with water and the copper(II) butanoate precursor at 120 °C for the compositions χ_{IL} = 0.95 (navy), χ_{IL} = 0.50 (blue) and χ_{IL} = 0.30 (cyan).

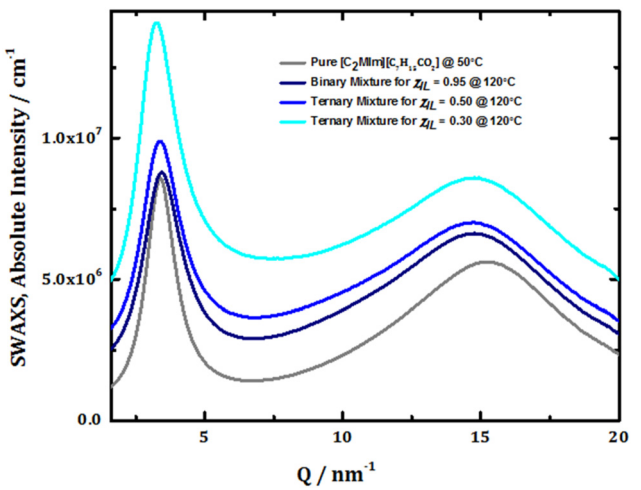

Fig. 16 SWAXS patterns of pure $[C_2MIm][C_7H_{15}CO_2]$ (grey), and its binary and ternary mixtures with water and the copper(II) octanoate precursor at 120 °C for the compositions χ_{IL} = 0.95 (navy), χ_{IL} = 0.50 (blue) and χ_{IL} = 0.30 (cyan).

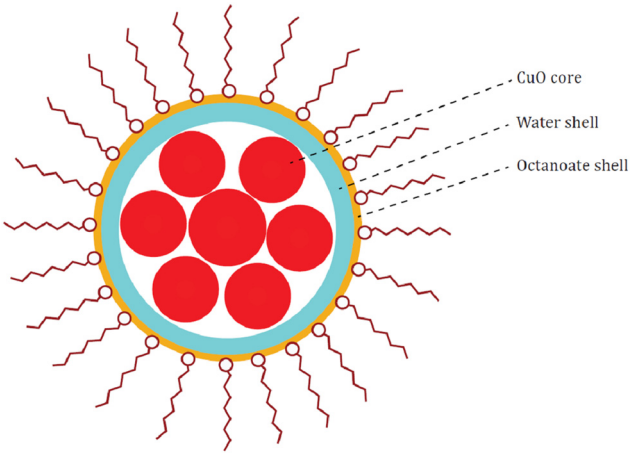

Fig. 17 Schematic view of CuO-NP formation in the $[C_2MIm][C_7H_{15}CO_2]$ IL and water mixture for one aggregation structure.

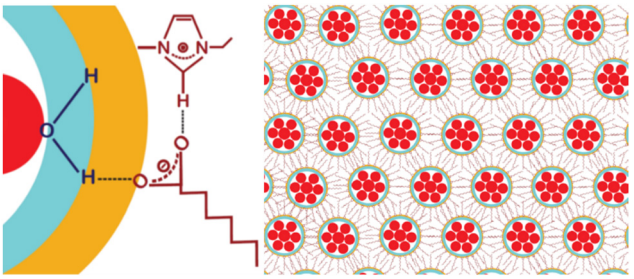

Fig. 18 Zoomed image of Fig. 17 with regard to the interaction involved in both shells between the $[C_2MIm][C_7H_{15}CO_2]$ IL and water molecules (left) and a schematic view of CuO-NP formation in the $[C_2MIm][C_7H_{15}CO_2]$ IL and water mixture for the whole aggregation (right).

at a short range, as schematised in Fig. 18, it was also tricky to visualise NPs using TEM. This can be explained by van der Waals forces, which are essential for well-organised solutions, and which are present to a greater extent in $[C_2MIm][C_7H_{15}CO_2]$ than in the other two ILs due to the presence of the long alkyl-chains.

However, the particles from the copper(II) butanoate precursor led to larger CuO-NPs that could be due to larger water shells or a non-existent water-shell. In fact, the $[C_2MIm][C_3H_7CO_2]$-IL is not as well-structured and could leave more free space for the copper salt. This could then leave more free space for the CuO-NPs to grow larger. In the case of the $[C_2MIm][CH_3CO_2]$-IL, there is no organisation observed for the pure IL (*cf.* Fig. 11), whereas there is an improvement of the solution organisation after the addition of copper salt and NP formation. This could explain why only clusters or very small CuO-NPs are found in the latter.

The combination of TEM, SAXS, and spectroscopy data suggests a proposed mechanism where water addition leads to partial dissociation of the IL ions, forming a water layer surrounded by the hydrophobic $[C_7H_{15}CO_2]^-$ anions. CuO nanoparticles subsequently form within the water layers, templated by the nanostructure of the IL (Fig. 17). The long octanoate chains likely coordinate to particle surfaces, limiting growth. The highly organised IL nanostructure provides defined regions for nanoparticle nucleation and growth, contributing to the narrow size distribution.

Experimental

Materials

The reagents used for the synthesis of ILs were supplied by Alfa Aesar [1-methyl-imidazole (99%)], Sigma Aldrich [diethyl-sulfate (98%), strontium hydroxide octahydrate (95%), butyric acid (99%), and octanoic acid (99%)] and Riedel-de Haën [acetic acid (99–100%)]. To study the physical properties, 1-ethyl-3-methyl-imidazolium hydroxide (99%) and 1-ethyl-3-methyl-imidazolium acetate (95%) were obtained from Io-litec. To carry out the neutron scattering experiment, deuterated reagents were purchased from QMX laboratories [acetic acid-d4 (98 atom% D) and octanoic acid-d16 (98 atom% D)]. Pure water at 18 MΩ was used for the mixtures.

Synthetic procedures for the ionic liquid 1-ethyl-3-methylimidazolium acetate, $[C_2MIm][CH_3COO]$

Acetic acid (15.87 g, 0.264 mol, 1 eq.) was combined with an excess of H_2O (20 cm^3) and added slowly to an aqueous solution of $[C_2MIm]OH$ (791.5 g, 0.264 mol, 1 eq.). The solution was stirred briefly and then reduced in volume *in vacuo* (rotary evaporator; 70 °C). When most of the water had been removed, ethanol was added (99%, 100 cm^3, large excess) in order to precipitate out any additional solid, and left to settle (4 °C, 12 h). The additional precipitate was removed *via* vacuum filtration using a 1.2 μm glass microfibre filter. The solvent was completely removed *in vacuo* (rotary evaporator; 70 °C) and the flask containing the liquid was transferred to a high vacuum line (80 °C; 3 days) leaving a golden viscous liquid (90%). Each batch was dried between 0.089 and 0.4035% according to the Karl Fisher titration. δ_H (300 MHz, D_2O) (ppm): 8.58 (1H, s, $NCHNC_2H_5$), 7.34 (1H, s, NCHCHN), 7.30 (1H, s, NCHCHN), 4.07 (2H, q, $N(CH_2)CH_3$), 3.75 (3H, s, NCH_3), 1.77 (3H, s, $O_2C(CH_3)$), 1.36 (3H, t, $N(CH_2)CH_3$). δ_C (75.4 MHz, D_2O) (ppm): 181.18, 136.31, 123.61, 122.20, 44.85, 35.77, 23.45, 14.81.

1-Ethyl-3-methylimidazolium butanoate, $[C_2MIm][C_3H_7COO]$

Butanoic acid (16.3 g, 0.185 mol, 1 eq.) was added slowly, drop-wise, to the colourless solution of $[C_2MIm]OH$ obtained previously (23.495 g, 0.185 mol, 1 eq.) until a pH of 8.7 was obtained using a Mettler Toledo MP220 pH meter. Ethanol (99%, 360 cm^3, large excess) was then added to help in azeotropic distillation of water. The solution was reduced in volume *in vacuo* (rotary evaporator; 70 °C); when most of the water had been removed, ethanol was added (99%, excess) in order to precipitate out any additional solid, left to settle (4 °C, 12 h). Any additional precipitate was removed *via* vacuum filtration using a 1.2 μm glass microfibre filter. The solution was again

reduced in volume *in vacuo* (rotary evaporator; 70 °C). If any precipitate was observed, it was removed again *via* vacuum filtration using a 1.2 μm glass microfibre filter. Additional absolute ethanol (small excess) was added, and the solvent was completely removed *in vacuo* (rotary evaporator; 70 °C) and the flask containing the liquid was transferred to a high vacuum line (80 °C; 3 days), leaving a golden viscous liquid (94%). Each batch was dried between 0.343 and 1.397% according to the Karl Fisher titration. δ_H (300 MHz, D_2O) (ppm): 8.59 (1H, s, $NCHNC_2H_5$), 7.35 (1H, s, NCHCHN), 7.31 (1H, s, NCHCHN), 4.07 (2H, q, $N(CH_2)CH_3$), 3.76 (3H, s, NCH_3), 2.01 (2H, s, $O_2C(CH_2)(CH_2)CH_3$), 1.41 (5H, m, $O_2C(CH_2)(CH_2)CH_3$), 0.75 (3H, t, $N(CH_2)CH_3$). δ_C (75.4 MHz, D_2O) (ppm): 184.21, 135.90, 123.79, 121.82, 45.11, 39.90, 35.70, 19.70, 14.82, 13.75.

1-Ethyl-3-methylimidazolium octanoate, $[C_2MIm][C_7H_{15}COO]$

Octanoic acid (18 g, 0.125 mol, 1eq.) was added slowly, dropwise, to the colourless solution of $[C_2MIm]OH$ (23.5 g, 0.185 mol, 1 eq.) obtained previously in step 3, until a pH of 8.82 was reached using a Mettler Toledo MP220 pH meter. Ethanol (99%, 150 cm^3, large excess) was then added to help in azeotropic distillation of water. The solution was reduced in volume *in vacuo* (rotary evaporator; 70 °C); when most of the water had been removed, ethanol was added (99%, 360 cm^3, large excess) in order to precipitate out any additional solid, left to settle (4 °C, 12 h). Any additional precipitate was removed *via* vacuum filtration using a 1.2 μm glass microfibre filter. The solution was again reduced in volume *in vacuo* (rotary evaporator; 70 °C). A precipitate was observed and any additional precipitate was removed *via* vacuum filtration using a 1.2 μm glass microfibre filter. The solution was reduced in volume *in vacuo* (rotary evaporator; 70 °C). Additional absolute ethanol (65 cm^3) was added, and the solvent was completely removed *in vacuo* (rotary evaporator; 70 °C) and the flask containing the liquid was transferred to a high vacuum line (80 °C; 3 days), leaving a golden viscous liquid (33 g, 70%). Each batch was dried between 0.1645 and 0.4005% according to the Karl Fisher titration. δ_H (300 MHz, D_2O) (ppm): 8.62 (1H, s, $NCHNC_2H_5$), 7.37 (1H, s, NCHCHN), 7.33 (1H, s, NCHCHN), 4.09 (2H, q, $N(CH_2)CH_3$), 3.77 (3H, s, NCH_3), 2.02 (2H, t, $O_2C(CH_2)$), 1.38 (5H, t, $O_2C(CH_2)_4(CH_2)$ (CH_2) CH_3)), 1.14 (8H, s, $O_2C(CH_2)(CH_2)_4(CH_3)$), 0.71 (3H, t, $N(CH_2)CH_3$). δ_C (75.4 MHz, D_2O) (ppm): 184.32, 135.47, 123.85, 122.28, 45.15, 38.07, 35.96, 31.50, 29.20, 28.73, 26.35, 22.43, 14.75, 13.83.

Synthetic procedures for the copper(II) carboxylate: Copper(II) butanoate synthesis

Copper hydroxide was dissolved in an excess of water and butanoic acid until a precipitate was formed. Diethyl ether was added to the solution to remove the excess of butanoic acid (two phases were formed, one containing the copper(II) butanoate mixed in diethyl ether and one containing water and an excess of butanoic acid). Then water was used to clean the diethyl ether/copper(II)butanoate phase. Copper(II)butanoate was then collected after decantation and filtration on filtrate paper and allowed to dry in a 60 °C oven.

Copper(II) octanoate synthesis

5 g of copper acetate was dissolved in an excess of water. An excess of octanoic acid was then added until a precipitate was formed. The precipitate was washed with cyclohexane as the copper octanoate obtained was found to be insoluble in water and partly soluble in diethylether. The product was then dried under high vacuum in an oil bath at 40 °C for almost 3 days.

Purification

Both products were recrystallised using hexane at room temperature and then put into a refrigerator for 24 hours. The products were then left in a desiccator.

IL-nanofluid synthesis

The synthesis was performed as described elsewhere.[22]

Transmission electron microscopy (TEM)

Transmission Electron Microscopy (TEM) images were acquired by bright field TEM, using a Tecnai 200 kV F20 Transmission Electron Microscope with a Field Emission Gun. The samples were prepared by diluting a drop of the nanofluid solution in dichloromethane (DCM) and left for a few minutes in an ultrasonic bath. A few drops of the sample were then pipetted onto an Agar holey carbon film copper TEM grid and washed with DCM. The prepared grid was set aside for *ca.* 20 minutes prior to inserting it into the microscope, in order to allow the solvent to evaporate. Images were taken with a Gatan CCD digital camera attached to the microscope.

Small and wide-angle X-ray scattering (SWAXS)

The SWAXS measurements were performed at the ESRF (European Synchrotron Radiation Facility, Grenoble, France) on the BM02-D2AM beamline. The incident photon energy was tuned to 11 keV which corresponds to a wavelength of λ = 1.12 Å. A two-dimensional detector, a CDD camera developed by Princeton, presently Ropper Scientific, was used. Two different distances between the sample and the detector were used to cover magnitudes of the scattering vector modulus (Q) from 0.06 to 20 nm^{-1}. The corresponding Bragg distances were from 0.3 to 100 nm. The magnitude of the scattering vector is defined as $Q = (4\pi/\lambda) \times \sin\theta$, where θ is half of the scattering angle and λ is the wavelength. In the short geometry, the distance from the sample to the detector was 16 cm, which covers the Q range from 1.1 to 20.4 nm^{-1}. In the long geometry, the distance from the sample to the detector was 164 cm, which covers the Q range from 0.06 to 1.56 nm^{-1}. The intensity curves measured with the long geometry were scaled to the absolute intensities with the aid of a laboratory calibrated Lupolen sample. The data measured with the short geometry were merged to the long measurements by matching of the data in the region 1.1–1.56 nm^{-1}. The scattered intensities were recorded for 20 or 50 s for SAXS, and 5, 10 or 20 s for SWAXS. The corrections of primary data were carried out using the software Bm2Img available on the beamline: (i) the dark current (*i.e.* non-illuminated camera), (ii) the flat field

response (*i.e.* homogeneously illuminated camera), and (iii) the tapper distortion. The standard silver behenate was used for the *Q*-range calibration. 2D images were converted into radial averages over the image centre to yield the scattered intensity *I vs.* the scattering vector *Q*. The contribution of the empty cell was subtracted from the scattering intensity of the studied samples. Quartz capillaries (2 mm in diameter with a wall thickness of 0.01 mm) from Hilgenberg were used as sample containers.

Density

Density was measured on a density meter, Mettler Toledo DM40, for each IL, as a function of temperature from 293.15 K to 363.15 K.

Viscosity

Viscosity was measured on a Malvern Bohlin Gemini 150 rheometer with a conic-plate system. Pure ILs and investigated mixtures were measured as a function of temperature from 293.15 K to 363.15 K.

Conductivity

Conductivity was measured on a HACH-Lange, SenslonTM + EC71, on the three pure ILs and their mixtures with water.

Zeta potential

Zeta potential measurements were attempted but were not successful due to the high viscosity of the ionic liquid solutions.

Crystallography

For the structures of compounds, X-ray intensity data were collected on an Agilent Supernova Dual Source diffractometer equipped with an Atlas CCD detector using CuK_α radiation (λ = 1.54184 Å) and ω scans. The images were interpreted and integrated with the program CrysAlisPro (Agilent Technologies).

Crystal data: $Cu_2(C_3H_7CO_2)_4$. M = 237.74 g mol^{-1}, triclinic, space group $P\bar{1}$ (no. 2), a = 5.15600(12) Å, b = 8.6547(3) Å, c = 11.5154(3) Å, α = 93.614(2)°, β = 93.5413(19)°, γ = 102.710(2)°, V = 498.76(2) Å^3, Z = 9, T = 293(2) K, μ(Cu-K$_\alpha$) = 10.582 mm^{-1}, D_{calc} = 2.773 g cm^{-3}, 9209 reflections measured (10.52° ≤ 2Θ ≤ 145.44°), and 1969 unique (R_{int} = 0.0299, R_{sigma} = 0.0182) were used in all calculations. The final R_1 was 0.0246 (>2σ(I)) and wR_2 was 0.0649 (all data).

$[C_2MIm]_2[Cu(C_3H_7CO_2)_4]$. M = 403.08 g mol^{-1}, triclinic, space group $P\bar{1}$ (no. 2), a = 14.3866(6) Å, b = 15.9472(9) Å, c = 17.1521(8) Å, α = 65.732(5)°, β = 77.128(4)°, γ = 67.803(5)°, V = 3310.9(3) Å^3, Z = 14, T = 100.00(10) K, μ(Cu-K$_\alpha$) = 1.346 mm^{-1}, D_{calc} = 1.269 g cm^{-3}, 22 643 reflections measured (8.4° ≤ 2Θ ≤ 145.24°), and 12 772 unique (R_{int} = 0.0375, R_{sigma} = 0.0573) were used in all calculations. The final R_1 was 0.0537 (>2σ(I)) and wR_2 was 0.1863 (all data).

$[C_2MIm]_2[Cu(C_7H_{15}CO_2)_4]$. M = 651.53 g mol^{-1}: triclinic, space group $P\bar{1}$ (no. 2), a = 17.1050(4) Å, b = 17.4308(6) Å, c = 18.9701(6) Å, α = 63.412(3)°, β = 86.315(2)°, γ = 76.256(3)°, V = 4907.3(3) Å^3, Z = 2, T = 99.9(2) K, μ(Cu-K$_\alpha$) = 1.027 mm^{-1}, D_{calc} = 1.161 g cm^{-3}, 84 986 reflections measured (9.982° ≤ 2Θ ≤ 133.198°), and 17 300 unique (R_{int} = 0.0553, R_{sigma} = 0.0392) were used in all calculations. The final R_1 was 0.1030 (I > 2σ(I)) and wR_2 was 0.2727 (all data).

$[C_4MIm][Cu_2(CH_3CO_2)_5]$. M = 235.74 g mol^{-1}; triclinic, space group $P1$ (no. 1), a = 8.0690(3) Å, b = 13.7637(5) Å, c = 16.3101(5) Å, α = 70.036(3)°, β = 89.552(3)°, γ = 89.760(3)°, V = 1702.49(10) Å^3, Z = 7, T = 100 K, μ(Cu Kα) = 2.854 mm^{-1}, D_{calc} = 1.610 g cm^{-3}, 6743 reflections measured (10.34° ≤ 2Θ ≤ 145.22°), and 5577 unique (R_{int} = 0.0170, R_{sigma} = 0.0319) were used in all calculations. The final R_1 was 0.0347 (>2σ(I)) and wR_2 was 0.0907 (all data).

Crystallization

Single crystals of $Cu_2(C_3H_7CO_2)_4$ were obtained by the recrystallization process using methanol, and single crystals of $[C_2MIm]_2[Cu(C_3H_7CO_2)_4]$, $[C_4MIm][Cu_2(CH_3CO_2)_5]$ and $[C_2MIm]_2[Cu(C_7H_{15}CO_2)_4]$ were obtained by the dissolution of copper(II) salt in their respective IL at 50 °C and left to recrystallise by slow cooling. A suitable crystal was then selected and placed on a diffractometer. The crystal was kept at 100 K during data collection. Using Olex2,[40] the structure was solved by direct methods using the ShelXS[41] structure solution program and refined by full-matrix least-squares on F^2 using the ShelXL[42] program package.

CCDC 2289136–2289139† contain the supplementary crystallographic data of the four crystal structures for this paper.

Conclusion

In this study, ionothermal synthesis of copper(II) carboxylates in their respective ILs resulted in the formation of either CuO clusters or nanoparticles (NPs). The basic anions function as both a base and stabilizing agent, facilitating the preparation of highly stable NP dispersions in ILs, known as nanofluids.

Distinct CuO-NP sizes were observed depending on the precursor used. The copper(II) octanoate precursor produced very small CuO-NPs, ranging from 10 to 25 nm, while the copper(II) butanoate precursor led to larger CuO-NPs, ranging from 10 to 61 nm. The smaller NPs obtained from the copper(II) octanoate precursor can be attributed to the high viscosity of the solution, which likely contributes to the slow and controlled production of uniformly shaped and smaller-sized NPs. The CuO nanofluids produced were highly stable, with no aggregation nor precipitation occurring even after months of storage, enabling their potential utilisation in applications.

Although the water concentration does not directly influence the NP size, as demonstrated by TEM analysis and the SWAXS study, it significantly impacts the physical properties of the resulting nanofluid, such as its conductivity. The versatility of these nanofluids offers the potential for their use in a wide range of applications, such as catalysis, energy storage, sensors, and antimicrobial coatings.

Conflicts of interest

There are no conflicts to declare.

Acknowledgements

We acknowledge the European Synchrotron Radiation Facility (ESRF) for provision of synchrotron radiation facilities (Experiment Number: 02-01-860) and we would like to thank Dr Cyrille Rochas for assistance and support in using beamline BM02-D2AM.

References

1 R. R. Kumar, K. U. Kumar and D. Haranath, in *Multifunctional Nanostructured Metal Oxides for Energy Harvesting and Storage Devices*, CRC Press, 2020.
2 A. Arora, V. Jaswal, K. Singh and R. Singh, *Orient. J. Chem.*, 2016, **32**, 2035–2042.
3 T. Tachikawa and T. Majima, *NPG Asia Mater.*, 2014, **6**, e100.
4 M. Fernández-García, A. Martínez-Arias, J. C. Hanson and J. A. Rodriguez, *Chem. Rev.*, 2004, **104**, 4063–4104.
5 G. R. Patzke, Y. Zhou, R. Kontic and F. Conrad, *Angew. Chem., Int. Ed.*, 2011, **50**, 826–859.
6 M. S. Chavali and M. P. Nikolova, *SN Appl. Sci.*, 2019, **1**, 607.
7 X. Yu, T. J. Marks and A. Facchetti, *Nat. Mater.*, 2016, **15**, 383–396.
8 A. Bhaumik, A. Haque, P. Karnati, M. F. N. Taufique, R. Patel and K. Ghosh, *Thin Solid Films*, 2014, **572**, 126–133.
9 N. M. Shaalan, T. Yamazaki and T. Kikuta, *Mater. Chem. Phys.*, 2011, **127**, 143–150.
10 S. G. Yang, T. Li, B. X. Gu, Y. W. Du, H. Y. Sung, S. T. Hung, C. Y. Wong and A. B. Pakhomov, *Appl. Phys. Lett.*, 2003, **83**, 3746.
11 B. Alenazi, A. Alsalme, S. G. Alshammari, R. A. Khan and M. R. H. Siddiqui, *J. Chem.*, 2020, **2020**, 1–11.
12 A. H. MacDonald, *Nature*, 2001, **414**, 409–410.
13 M. Armand, M. Armand, F. Endres, D. R. MacFarlane, H. Ohno and B. Scrosati, *Nat. Mater.*, 2009, **8**, 621–629.
14 D. Freudenmann, S. Wolf, M. W. Wolff and C. Feldmann, *Angew. Chem., Int. Ed.*, 2011, **50**, 11050–11060.
15 A. Taubert, in *Encyclopedia of Inorganic and Bioinorganic Chemistry*, John Wiley & Sons, Ltd, 2016, pp. 1–14.
16 C. Verma, E. E. Ebenso and M. A. Quraishi, *J. Mol. Liq.*, 2019, **276**, 826–849.
17 O. Renier, G. Bousrez, M. Yang, M. Hölter, B. Mallick, V. Smetana and A.-V. Mudring, *CrystEngComm*, 2021, **23**, 1785–1795.
18 E. Ahmed, E. Ahmed, E. Ahmed and M. Ruck, *Angew. Chem., Int. Ed.*, 2012, **51**, 308–309.
19 J. Richter and M. Ruck, *Molecules*, 2019, **25**, 78.
20 Z. He and P. Alexandridis, *Phys. Chem. Chem. Phys.*, 2015, **17**, 18238–18261.
21 W. Yu and H. Xie, *J. Nanomater.*, 2012, **2012**, 1–17.
22 M. Karimi-Nazarabad, E. K. Goharshadi, M. H. Entezari and P. Nancarrow, *Microfluid. Nanofluid.*, 2015, **5**, 1191–1202.
23 J. Li, X. Zhang, B. Xu and M. Yuan, *Int. Commun. Heat Mass Transfer*, 2021, **127**, 105543.
24 F.-L. Chen, I.-W. Sun, H.-P. Wang and C.-H. Huang, *J. Nanomater.*, 2009, **2009**, 1–4.
25 K. Lunstroot, L. Baeten, L. Baeten, L. Baeten, P. Nockemann, J. A. Martens, P. Verlooy, X. Ye, C. Görller-Walrand, K. Binnemans and K. Driesen, *J. Phys. Chem. C*, 2009, **113**, 13532–13538.
26 F. C. C. Oliveira, L. M. Rossi, R. F. Jardim and J. C. Rubim, *J. Phys. Chem. C*, 2009, **113**, 8566–8572.
27 M. Zhao, N. Li, L. Zheng, G. Li and L. Yu, *J. Dispersion Sci. Technol.*, 2008, **29**, 1103–1105.
28 J. Hu, X. Hu, A. Chen and S. Zhao, *J. Alloys Compd.*, 2014, **603**, 1–6.
29 V. Khare, A. Kraupner, A. Mantion, A. Jeličić, A. F. Thünemann, A. F. Thünemann, C. Giordano and A. Taubert, *Langmuir*, 2010, **26**, 10600–10605.
30 M. Swadźba-Kwaśny, L. Chancelier, S. Ng, H. G. Manyar, C. Hardacre and P. Nockemann, *Dalton Trans.*, 2012, **41**, 219–227.
31 J. Jacquemin, M. Anouti and D. Lemordant, *J. Chem. Eng. Data*, 2011, **56**, 556–564.
32 M. Anouti, J. Jones, A. Boisset, J. Jacquemin, M. Caillon-Caravanier and D. Lemordant, *J. Colloid Interface Sci.*, 2009, **340**, 104–111.
33 F. C. Strobridge, N. Judaš and T. Friščić, *CrystEngComm*, 2010, **12**, 2409–2418.
34 A. Hinz and M. Köckerling, *Z. Anorg. Allg. Chem.*, 2015, **641**, 1347–1351.
35 M. Anouti, A. Mirghani, J. Jacquemin, L. Timperman and H. Galiano, *Ionics*, 2013, **19**, 1783–1790.
36 V. Khare, Z. Li, A. Mantion, A. A. Ayi, S. Sonkaria, A. Voelkl, A. F. Thünemann and A. Taubert, *J. Mater. Chem.*, 2010, **20**, 1332–1339.
37 A. Martinelli, M. Maréchal, Å. Östlund and J. Cambedouzou, *Phys. Chem. Chem. Phys.*, 2013, **15**, 5510.
38 U. Salma, P. Ballirano, M. Usula, R. Caminiti, N. V. Plechkova, K. R. Seddon and L. Gontrani, *Phys. Chem. Chem. Phys.*, 2016, **18**, 11497–11502.
39 C. C. Weber, N. J. Brooks, F. Castiglione, M. Mauri, R. Simonutti, A. Mele and T. Welton, *Phys. Chem. Chem. Phys.*, 2019, **21**, 5999–6010.
40 O. V. Dolomanov, L. J. Bourhis, R. J. Gildea, J. a. K. Howard and H. Puschmann, *J. Appl. Crystallogr.*, 2009, **42**, 339–341.
41 G. M. Sheldrick, *Acta Crystallogr., Sect. A: Found. Crystallogr.*, 2008, **64**, 112–122.
42 G. M. Sheldrick, *Acta Crystallogr., Sect. C: Struct. Chem.*, 2015, **71**, 3–8.

